My name is Jeffrey Uncu (jeffrey.uncu@mail.utoronto.ca, University of Toronto), I am from Professor Nicolas Grisouard's (nicolas.grisouard@utoronto.ca, University of Toronto) group at the University of Toronto. My co-author and I are pleased to submit this manuscript titled "Wave Scattering by an Isolated Cyclogeostrophic Vortex". This paper is a non-peer reviewed preprint submitted to EarthArXiv. We have submitted to the Journal of Fluid Mechanics for peer review on February 21, 2024.

# Wave Scattering by an Isolated Cyclogeostrophic Vortex

**J. Uncu† and N. Grisouard**

Department of Physics, University of Toronto, Toronto, ON M5S 1A7, Canada

(Received xx; revised xx; accepted xx)

The propagation paths of oceanic internal tides are influenced by their interactions with vortices. We examine the scattering effect that an isolated vortex in (cyclo)geostrophic balance has on a rotating shallow-water plane wave. We run a suite of simulations in which we vary the non-dimensional vorticity of the vortex, $Ro$, the relative scale of the vortex size to the Rossby radius of deformation, $Bu$, and the size of the vortex compared to the plane wave wavelength, $K$. We compare the scattered wave flux pattern to ray-tracing predictions. Ray tracing predictions are relatively insensitive to $K$ in the $1 < K < 4$ range we investigate; however, they generally underestimate the broad angles of the shallow-water wave scattering patterns, especially for the lower end of the $K$ range. We then measure the ratio of the scattered wave energy flux to the incoming wave energy flux, denoted as $S$ for each simulation. We find that $S$ follows a power law $S \propto (FrK)^2$ when $S < 0.2$, where $Fr = Ro/\sqrt{Bu}$ is the Froude number. When $S > 0.2$, it plateaus following a sigmoid.

† Email address for correspondence: jeffrey.uncu@mail.utoronto.ca

**Abstract must not spill onto p.2**

## 1. Introduction

When the barotropic tide oscillates over the bathymetry of the ocean, it creates internal tides (ITs). These are internal waves that oscillate at or near the generating tidal frequencies (Garrett & Kunze 2007). Of the 4 TW that are injected into the ocean by astronomical forcing, approximately 2.4 TW are transferred to ITs (Egbert & Ray 2003). Most of their energy is lost to turbulent mixing at the generation sites, while about 10-40% propagate away (Egbert & Ray 2000). Low modes can propagate thousands of kilometres, making the details of their horizontal propagation critical to determining where they will eventually dissipate (Zhao *et al.* 2016). This makes them an essential aspect for forecasting climate and tuning general circulation models (de Lavergne *et al.* 2019).

Unlike the barotropic tide, which oscillates in phase with astronomical forcing, IT features are more susceptible to evolve as a result of changing ocean conditions throughout its propagation (Nash *et al.* 2012). These changes include evolving local stratification, and, of note for this study, eddies. At mid-latitudes, mesoscale eddies ($\sim$ 100 km wide) are well described by quasi-geostrophic models. These are flows with negligible advective effects, and whose dynamic evolution is dominantly characterised by a balance between Coriolis and pressure forces, which leads us to hereafter refer to these flows as 'balanced'. They feature small Rossby numbers $Ro = U/(Lf)$, where $U$ and $L$ are characteristic eddy velocity and length scales, respectively, and $f$ is the local Coriolis parameter.

Advances in satellite altimetry in the 1990s, starting with the TOPEX/Poseidon mission, provided the first global visualisations of large-scale currents and of the mesoscale eddy field (Fu *et al.* 1994). This allowed Rainville & Pinkel (2006) to calculate the propagation paths of mode-1 to mode-5 ITs using ray-tracing. They also show that higher modes are more susceptible to phase shifts by the balanced flow, causing an apparent loss in IT energy when measured by harmonically filtering narrow bands around the tidal frequencies. However, ray tracing assumes that the IT horizontal wavelength $\lambda$ is small compared to the length scale of variations in the eddy velocity $L$. Mesoscale eddies usually have length scales smaller than the largest mode-1 semi-diurnal tides at mid-latitudes, but are typically larger than higher IT modes. As such, ray tracing is effective only for higher modes in principle, but is often used when length scales are similar. Chavanne *et al.* (2010) used 3D ray tracing to model wave propagation of an IT with a 50 km wavelength through a 55 km vortex inspired by a vortex near the Hawaiian ridge. They showed that even near generation sites, the IT can become very incoherent, that is, it can develop significant and time-evolving phase shifts with the astronomical forcing. They also showed that IT energy could be amplified up to a factor of 15 in the core of the vortex.

New remote sensing satellites, such as the Surface Water and Ocean Topography (SWOT) mission (Morrow *et al.* 2019) resolve scales up to a few tens of kilometres. The increased resolution should enable us to observe higher Rossby numbers and shorter IT wavelengths, prompting researchers to use new techniques to further refine the mapping of ITs that do not use the ray tracing assumption. One such technique is the kinetic equation developed in Savva & Vanneste (2018), Kafiabad *et al.* (2019) and Savva *et al.* (2021) that models the redistribution of inertia-gravity wave energy in position-wavenumber phase space when embedded in quasi-geostrophic turbulence. This method, however, requires a small Rossby number. A powerful deterministic method that does not assume length scale separation and is capable of handling $O(1)$ Rossby numbers is triad resonance theory (TRT). Ward & Dewar (2010) used TRT to describe the evolution of a wave mode wave embedded in a balanced flow in the one-layer rotating shallow-water equations (RSWEs). In this interaction, the balanced flow provides a pathway for the waves to exchange energy with other waves of constant frequency. This method clearly illustrates how the advection term couples the balanced mode and wave mode to force the linear equations of motion at resonant wave modes. This so-called 'catalytic interaction' of a PV mode and two wave modes was first described in Lelong & Riley (1991) and later in Bartello (1995). However, as the Rossby number increases and the duration of the scattering process increases, near-resonant triads and higher-order non-linearities become increasingly significant, and thus, a solution that only considers resonant triads becomes increasingly inaccurate.

In this article, we model the interaction between an isolated balanced cyclogeostrophic vortex and a Poincaré wave by numerically solving the single-layer RSWEs. This allows us to explore the parameter space spanned by Rossby numbers that range from very small to $O(1)$ values, vortex scales that widely straddle the Rossby radius of deformation, and Poincaré wavelengths that are four times smaller than the vortex scale to as large as the vortex. We first qualitatively compare the scattered wave flux to ray-tracing predictions. We then calculate the amount of energy that is transferred from the incoming wave to the scattered waves for each simulation and then find the scaling relations given the wave and vortex parameters. These interactions are expected to be ubiquitous in the ocean, with applications for diagnosing processes in global circulation models and satellite altimetry data.

## 2. Methods

### 2.1. *Physical and mathematical setup*

Here, we describe our equations and the processes we model, which we summarise in figure 1.

We solve the RSWEs on a square domain of side length $L_x$, with which we associate a Cartesian coordinate system $(x, y)$ centred in the middle of the domain. The layer is under gravitational acceleration $g$, has depth at rest $H$, and rotates as an $f$-plane. These parameters define a non-rotating speed $c_0 = \sqrt{gH}$ and a Rossby radius of deformation $L_d = c_0/f$. The

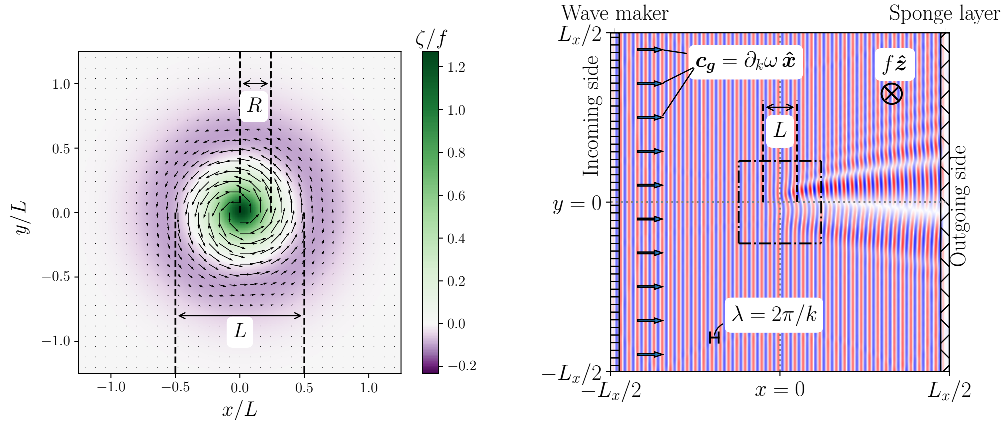


(a) (b)

Figure 1: Setup for the simulation with parameters $\mathrm{Ro}_\zeta = -1.27$, $\mathrm{Bu} = 1.76$, $K = 3.0$. (a) Normalised vorticity field for an isolated anticyclonic cyclogeostrophic vortex. Black arrows represent the vortex velocity vectors. (b) Height field for a Poincaré wave that is forced from the left side of the domain and interacts with the isolated vortex pictured in (a). The black dash-dotted square in (b) aligns with the bounds of panel (a).

forced-dissipated one-layer RSWEs are

$$\partial_t \boldsymbol{u} + \boldsymbol{u} \cdot \boldsymbol{\nabla} \boldsymbol{u} + g \boldsymbol{\nabla} h + f \hat{\boldsymbol{z}} \times \boldsymbol{u} - \mu \boldsymbol{\nabla}^4 \boldsymbol{u} = \boldsymbol{F}_w(x,t) + \boldsymbol{S}_w(x) \quad \text{and} \tag{2.1a}$$

$$\partial_t h + h \boldsymbol{\nabla} \cdot \boldsymbol{u} + \boldsymbol{u} \cdot \boldsymbol{\nabla} h - \mu \boldsymbol{\nabla}^4 h = F_h(x,t) + S_h(x), \tag{2.1b}$$

where $\boldsymbol{u} = (u, v)$ is the horizontal velocity field, $\boldsymbol{\nabla} = (\partial_x, \partial_y)$ is the horizontal del operator, $\mu$ is the kinematic hyperviscosity, and $h$ is the height of the total water column. The terms $\boldsymbol{F}_w$, $\boldsymbol{S}_w$, $F_h$ and $S_h$ on the right-hand sides are wave forcing and sponge layer terms, which we describe in more detail later.

Our initial condition consists of an axisymmetric circular vortex centred at the origin of the domain. We achieve this through a three-step process. (i) First, we create a Gaussian vortex in geostrophic balance following

$$\left[u_\Theta^{(0)},\ h_\Theta^{(0)}\right] = \left[\pi^2 f r,\ \frac{H}{Bu_0}\right] Ro \exp\left(-\frac{r^2}{2(L/\pi)^2}\right), \tag{2.2}$$

where $u_\Theta^{(0)}$ and $h_\Theta^{(0)}$ are the initial tangential velocity and height fields of this vortex, $L$ its characteristic width, $Bu_0 = (L_d/L)^2$ is the Burger number, and $r$ is the distance from the centre of the vortex. While Eq. (2.2) is a relatively good approximation for a quasi-geostrophic vortex, water parcels in a vortex with higher $Ro$ experience a significant centrifugal acceleration, which modifies the balance. Applying the iterative method of Penven *et al.* (2014), which we detail in Appendix A, to Eq. (2.2) yields velocity fields $u_\Theta^{(1)}$ and $h_\Theta^{(1)}$ that are one step closer to achieving cyclogeostrophic balance. We then use these velocity and height fields as initial conditions for an unforced RSWE simulation. After a transitory adjustment in the form of waves radiating from the vortex and dissipated by additional sponge layers (see Appendix B), and a rearrangement of the water parcels, a stationary vortex remains. Finally, we save the velocity and height fields $u_\Theta^{(2)}$ and $h_\Theta^{(2)}$ to be used later as initial conditions for our forced simulations. We repeat this procedure for as many initial vortices as we need. For all simulations, $L = 25$ km and $f = -10^{-4}$ s$^{-1}$.

The adjusted vortex length is defined as $L_a = \pi R$, where $R$ is the radius of the maximum tangential velocity $U_q = u_\Theta^{(2)}(R)$, as shown in figure 1a. We define its vorticity Rossby number and bulk Rossby number as

$$Ro_\zeta = \left.\frac{\zeta}{f}\right|_{x=y=0} \quad \text{and} \quad Ro_b = \frac{U_q}{L_a f}, \tag{2.3}$$

respectively, where $\zeta = \partial_x v - \partial_y u$ is the vertical vorticity (note that at this point, no other form of motion is present in the domain).

The resultant azimuthal velocity and vorticity profiles are shown in figure 2. For a given value of $Ro_b$, cyclogeostrophic balance makes the cyclonic vortices wider than their geostrophic counterparts. For a cyclonic vortex in the southern hemisphere, the inward pressure gradient must balance not only the outward Coriolis force, but also the centrifugal force. Thus, a decrease in velocities near the initialised geostrophic value of $U_q$ is needed to achieve balance, leading to a wider shape. On the other hand, for anticyclonic vortices, the

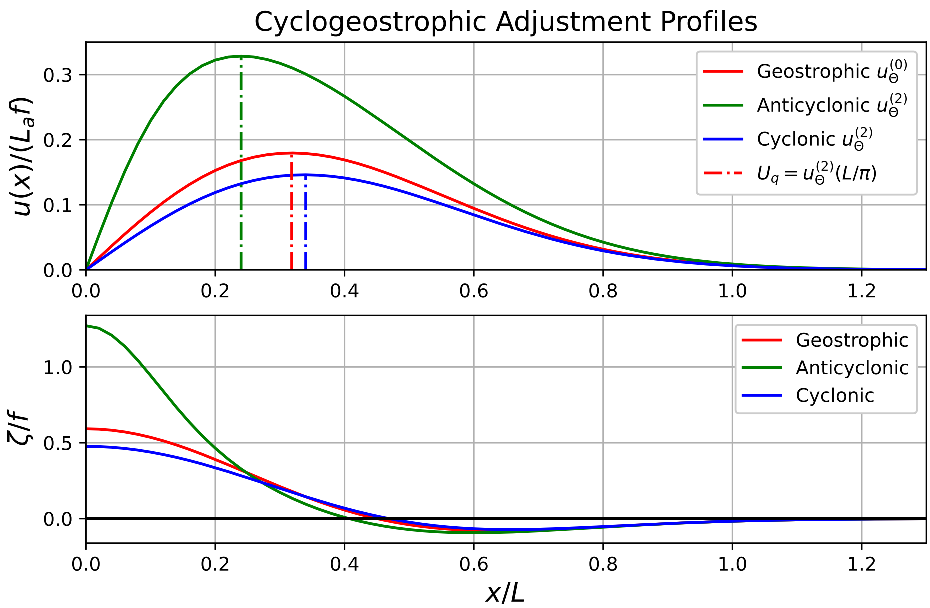


Figure 2: Azimuthal velocity profiles of a pair of cyclonic (solid blue) and anticyclonic (solid green) vortices that originally started from the same geostrophically-balanced velocity profile (solid red) with bulk Rossby number $Ro_b = 0.18$. The final normalised velocity profiles are shown in the upper figure, and the normalised vorticity profiles are shown in the lower figure. The vertical dashed-dotted lines correspond to the position $x = R$, where velocity is maximum. The anticyclonic profiles are flipped over the $x$-axis to easily compare with the cyclonic profiles.

centrifugal force and pressure gradient are outward and balance the inward Coriolis force. Thus, the velocity increases, leading to a narrower profile (Shakespeare 2016).

In order to capture this cyclonic/anticyclonic asymmetry in the cyclogeostrophic vorticity distributions, which the bulk Rossby number misses, we also measure the enstrophy, $\varepsilon$, of each vortex, defined below as the integral of the square of the vorticity,

$$\varepsilon' = \iint \zeta^2 \,\mathrm{d}x\,\mathrm{d}y. \tag{2.4}$$

Enstrophy is a convenient method for measuring the strength of the vortex for two reasons. First, the vorticity is the most relevant quantity for scattering. This is expected from ray-tracing theory, which predicts that at leading order in vortex velocity $U$, the vortical part of the mean flow will rotate the wave vector $\boldsymbol{k}$, while the divergent part will only affect the ray paths at a higher order (Bühler 2014, § 4.4.3). This rotation of the wave vector is the main form of scattering that we expect in our experiments. This is consistent with TRT which dictates that the dominant triad interaction between the vortex and the wave flow produces a discrete rotation of the wave vector. Second, enstrophy integrates the vorticity over the whole domain and therefore captures some of the information about the spatial structure of the anticyclonic and cyclonic profiles created after cyclogeostrophic adjustment. We non-dimensionalise enstrophy with $\varepsilon = \varepsilon'/(L_a^2 f^2)$.

We then generate a plane wave on the boundary at $x = -L_x/2$, hereafter referred to as the "incoming side". It propagates along $x$ with wavenumber $\boldsymbol{k}_i = (2\pi\lambda^{-1}, 0)$, where $\lambda$ is the wavelength, and frequency $\omega_0 = \sqrt{f^2 + c_0^2 k_i^2}$ with corresponding period $P = 2\pi\omega_0^{-1}$. We generate this wave via the forcing terms

$$\boldsymbol{F}_w = \tau_w^{-1}\left(\boldsymbol{U}_w - \boldsymbol{u}\right)\Pi_w \quad \text{and} \quad F_h = \tau_w^{-1}\left(H_w - h\right)\Pi_w, \tag{2.5}$$

which first appeared in Eqs. (2.1), where $\tau_w = P$ is the wave restoration time scale. In these forcing terms, the fields $(\boldsymbol{u}, h)$ are restored to values $(\boldsymbol{U}_w, H_w)$ that satisfy the polarisation relations for Poincaré waves (see Appendix C), that is,

$$\boldsymbol{U}_w = Fr_w c_0 \left(1, \frac{\omega_0}{f}\right)\cos(kx - \omega_0 t) \quad \text{and} \quad H_w = \frac{kH}{f}\sin(kx - \omega_0 t), \tag{2.6}$$

where $Fr_w = U_w/c_0$ is the wave Froude number, which we keep small throughout this article to keep the waves linear. This forcing occurs over a limited spatial window along $x$, following

$$\Pi_w = \Pi\left(x, -L_x/2\right), \tag{2.7}$$

where $\Pi(x, x_0)$ is a Tukey window that we detail in Appendix B.

At the boundary $x = +L_x/2$, hereafter referred to as the "outgoing side", a sponge layer absorbs waves through the sponge terms

$$\boldsymbol{S}_w = -\tau_s^{-1}\boldsymbol{u}\Pi_s \quad \text{and} \quad S_h = \tau_s^{-1}(H-h)\Pi_s, \quad \text{where} \quad \Pi_s = \Pi[x, L_x/2-\lambda], \tag{2.8}$$

and $\tau_s = 0.05P$ is the sponge restoration time scale. We verified that the vortex remains unaffected by the wave: for our purposes, it does not move, deform, lose, or gain energy in any detectable manner. The result is a time-independent scattering amplitude pattern induced by the vortex shown in figure 1b.

### 2.2. *Numerical setup and experimental design*

We use Dedalus (Burns *et al.* 2020) to solve the RSWEs spectrally with periodic boundaries in the horizontal directions. We use 512 points in each direction with a uniform spacing of $dx = L/50$. The time step is determined by the vortex strength using the CFL condition $dt < 10^{-2}dx/|U_q|$. The simulation time for each experiment is $t_s = 4t_T/3$, where $t_T = L_x k/\omega_0$ is the transit time of the wave phase across the domain. In practice, the phase and group speeds of the incoming waves are similar in magnitude, and thus $t_T$ is sufficient time for the wave packets to reach the other side of the domain.

To initialise the simulations, we define the unadjusted ratio of the vortex length scale to the wavelength of the incoming wavelength $K_0 = L/\lambda$, which we vary from 0 to 4. In doing so, we test the consequences of violating the traditional ray-tracing assumption, which requires $K_0 \gg 1$. Similarly, we initialise the unadjusted Burger number as $Bu_0 = (L_d/L)^2$ from 0.5 to 1.5. McWilliams (2016) noted that the size of realistic vortices is around the radius of deformation $L_d$. However, we find that they are stable at various scales and explore multiple regimes for completeness. Due to the different adjustment processes between cyclonic and anticyclonic vortices, for a given initial $L$, the adjusted length scale ratio $K = L_a/\lambda$ is not the same for the cyclonic and anticyclonic simulations. In the end, $K$ ranges from 0.5 to 4.5, and similarly, the adjusted Burger numbers $Bu = (L_d/L_a)^2$ range between 0.43 to 2.6. We

| Parameter | Anticyclonic | Cyclonic |
|---|---|---|
| $Ro_\zeta$ | $-1.27, -0.54, -0.22, -0.13$ | $0.18, 0.47, 0.60, 0.89$ |
| $Ro_b$ $(\times 100)$ | $-10.46, -5.07, -2.16, -1.19$ | $1.80, 4.65, 5.98, 7.96$ |
| $\varepsilon$ $(\times 100)$ | $19.02, 4.39, 0.80, 0.24$ | $0.55, 3.71, 6.12, 11.01$ |
| $Bu(L_a/L)^2 = Bu_0$ | $0.5, 0.9, 1.0, 1.1, 1.5$ | $0.5, 0.9, 1.0, 1.1, 1.5$ |
| $K(L_a/L)^{-1} = K_0$ | $1, 1.5, 2, 3, 4$ | $1, 1.5, 2, 3, 4$ |

Table 1: Simulation parameters shown as intialisation before adjustments are made.

use vortices whose values for $Ro_\zeta$ vary from $-1.27$ to $0.89$. We keep $Fr_w < 10^{-3}$ for all simulations to avoid non-linear steepening and wave-wave interactions between the different components of the incoming and scattered waves. Our suite of simulations consists of all combinations of the Rossby numbers, Burger numbers, and length scale ratios shown in table 1, resulting in a total of 200 simulations.

### 2.3. *Diagnostics*

In this section, we show how to extract the scattered wave fields from the simulation outputs. We then demonstrate how to calculate the phase-averaged flux and outline the process for calculating the ratio of wave energy scattered by the vortex.

Because the vortex does not evolve during the course of our simulations, we extract the wave field $(\boldsymbol{u}_w, h_w)$ simply by subtracting the initial conditions from the simulation output, that is, $\boldsymbol{u}_w = \boldsymbol{u} - \boldsymbol{u}_\Theta^{(2)}$ and $h_w = h - h_\Theta^{(2)}$. After the wave has reached the sponge layer, the sub-domain defined by a square of length $4L$ centred at the origin will have a wave field pattern that is constant in time if averaged over one period $P$. We define the phase-averaged energy flux density with

$$\boldsymbol{\phi}_X = \frac{1}{2} c_0^2 \boldsymbol{u}_X \eta_X \quad \text{and} \quad \overline{\boldsymbol{\phi}}_X = \frac{1}{P} \left| \int_{t_p}^{t_p+P} \boldsymbol{\phi}_X \, \mathrm{d}t \right|, \tag{2.9}$$

where $\eta_X = h_X - H$ and $t_p > 0.9t_T$, which ensures the wave has propagated past the vortex but has not yet wrapped around the periodic boundaries. The subscript $X$ denotes which field is used. For example, $X = w$ denotes the phase-averaged total wave flux $\overline{\boldsymbol{\phi}}_w$, which we show in figure 3a for a typical total wave field.

To isolate only the flux of the scattered waves $\overline{\boldsymbol{\phi}}_s$ shown in figure 3b, we take a 2D Fourier transform of $u_w$, $v_w$, and $h_w$ and cancel the amplitudes of the Fourier modes whose wave vectors are parallel to the incoming wave vector $\boldsymbol{k}_i$. We then take an inverse Fourier transform to obtain $u_s$, $v_s$, and $h_s$, which we use to calculate $\overline{\boldsymbol{\phi}}_s$ using equation (2.9).

To calculate the ratio of scattered wave flux to incoming wave flux, we define the control volume shown in figure 3, which is made up of four boundaries located away from the vortex. The incoming boundary is placed at $x/L = -2$, spans $-2 \leqslant y/L \leqslant 2$, and has unit normal vector $\boldsymbol{n}_{in} = (-1,\ 0)$. Given that we observe the backscatter to be negligible, all of the energy enters through this boundary. We define the outgoing boundary as a semicircle in the $x > 0$ half-plane, centred around the origin, of radius $x/L = 2$, where virtually all of the energy exits. We denote $\boldsymbol{n}_{out}$ as the unit vector normal to this boundary. There is virtually no energy moving through the top and bottom boundaries shown in dashed blue lines.

The total incoming and scattered fluxes are then

$$\Phi_{in} = \int \overline{\boldsymbol{\phi}}_w \cdot \boldsymbol{n}_{in}\, \mathrm{d}s \qquad \text{and} \qquad \Phi_s = \int \overline{\boldsymbol{\phi}}_s \cdot \boldsymbol{n}_{out}\, \mathrm{d}s, \tag{2.10}$$

integrated along the incoming and outgoing boundaries, respectively. To compare how much energy is scattered between simulations, we define the scattering ratio as

$$S = \Phi_s / \Phi_{in}. \tag{2.11}$$

We will calculate this quantity for all simulations in the next section, and use scaling laws to draw a relation from the non-dimensional variables to $S$.

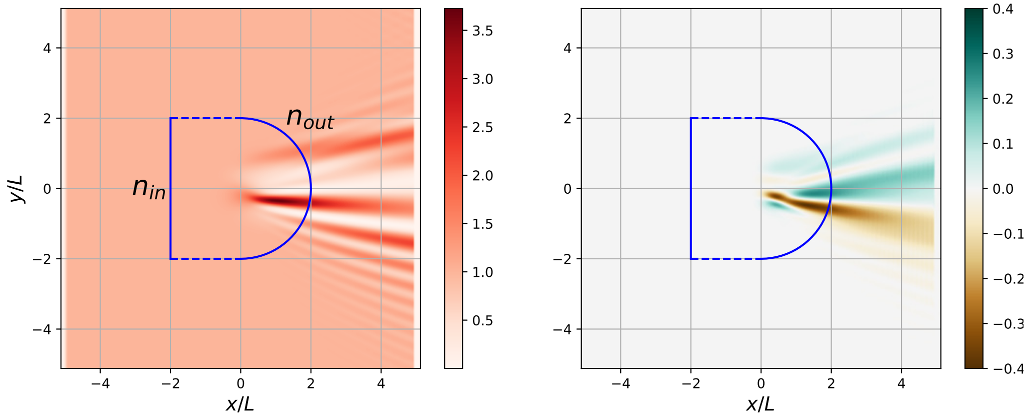


(a) Full wave field $\overline{\boldsymbol{\phi}}_w$.

(b) $y$ component of $\overline{\boldsymbol{\phi}}_s$.

Figure 3: Phase-averaged wave flux for $(Ro_\zeta, Bu, K) = (0.60, 0.44, 4.3)$. The solid blue lines in the control volume are used to calculate the ratio $S$ of the scattered wave flux to the incoming wave flux. The vector $\boldsymbol{n}_{in}$ ($\boldsymbol{n}_{out}$) is the unit vector associated with the incoming (outgoing) boundary.

## 3. Results

### 3.1. *Scattering Pattern*

The pattern of the wave flux density magnitude $|\overline{\boldsymbol{\phi}}_w|$, shown in figure 3a, consists of an alternating 'constructive/destructive' interference pattern in the $x > 0$, $y < 0$ quadrant, with the strongest flux values to be found near the exit of the vortex centre. In the $x > 0$, $y > 0$ quadrant, there is a less well-defined scattering pattern. This qualitatively matches the alternating flux pattern of Dunphy & Lamb (2014) for a barotropic vortex. We see that there are regions on the outgoing side of the vortex where the flux has dropped to near-zero and regions where the flux is more than three times that of the incoming wave.

To explain these features, we show the $y$-component of the scattered wave flux density, $\overline{\boldsymbol{\phi}}_s \cdot \hat{\boldsymbol{y}}$, in figure 3b. Indeed, isolating the scattered part of the wave field eliminates the distracting interference pattern with the unscattered wave. The $y$-component helps us distinguishing three scattered beams. The first one, heareafter referred to as the central scattered beam (CSB), crosses the centre of the vortex. In the cyclonic case presented in figure 3, this beam is characterised by $\overline{\boldsymbol{\phi}}_s \cdot \hat{\boldsymbol{y}} < 0$. The other two beams emanate from the flanks of the vortex and have $\overline{\boldsymbol{\phi}}_s \cdot \hat{\boldsymbol{y}} > 0$. We hereafter refer to these beams as right and left scattered beams (RSB and LSB, respectively), in reference to whether they approach the left or right flank of the vortex with respect to the direction of incident wave propagation.

We can now interpret that the region where we see a maximum in $|\overline{\boldsymbol{\phi}}_s|$ is where constructive interference between the RSB and the CSB takes place. The regions where we find zero flux are created by the RSB and CSB destructively interfering. In experiments with strong vortices, we find lines of destructive interference due to a 180° phase difference between BSW and CSW.

We claim that the scattering direction is mostly controlled by the vorticity. In our simulations, the Coriolis parameter is negative, so the negative (positive) vorticity in the centre of the (anti)cyclonic vortex produces the CSB moving to the right (left) of the incident propagation direction, and the opposite-sign vorticity region on the outside (recall figure 1a) produces the LSB and RSB. To support this claim, we now compare this pattern with the predictions from ray-tracing equations, which we recall in Appendix D, for an anticyclonic and cyclonic vortex of similar $|Ro_\zeta|$ and two different values of $K$.

Figure 4 shows that ray tracing captures the "left, right, left" scattered beam direction pattern for cyclonic vortices and the "right, left, right" pattern for anticyclonic vortices. There are small differences in the ray tracing results when we compare cyclonic and anticyclonic vortices that are more than just a flip over the $y = 0$ axis for two reasons. First, anticyclonic vortices are "slimmer" (vorticity is more concentrated near the centre, over a shorter radius) compared to cyclonic vortices. Second, the refractive effects due to the height field in the term $d\omega/d\boldsymbol{x}$ in equation (D 1) differ between cyclonic and anticyclonic vortices. Indeed, an

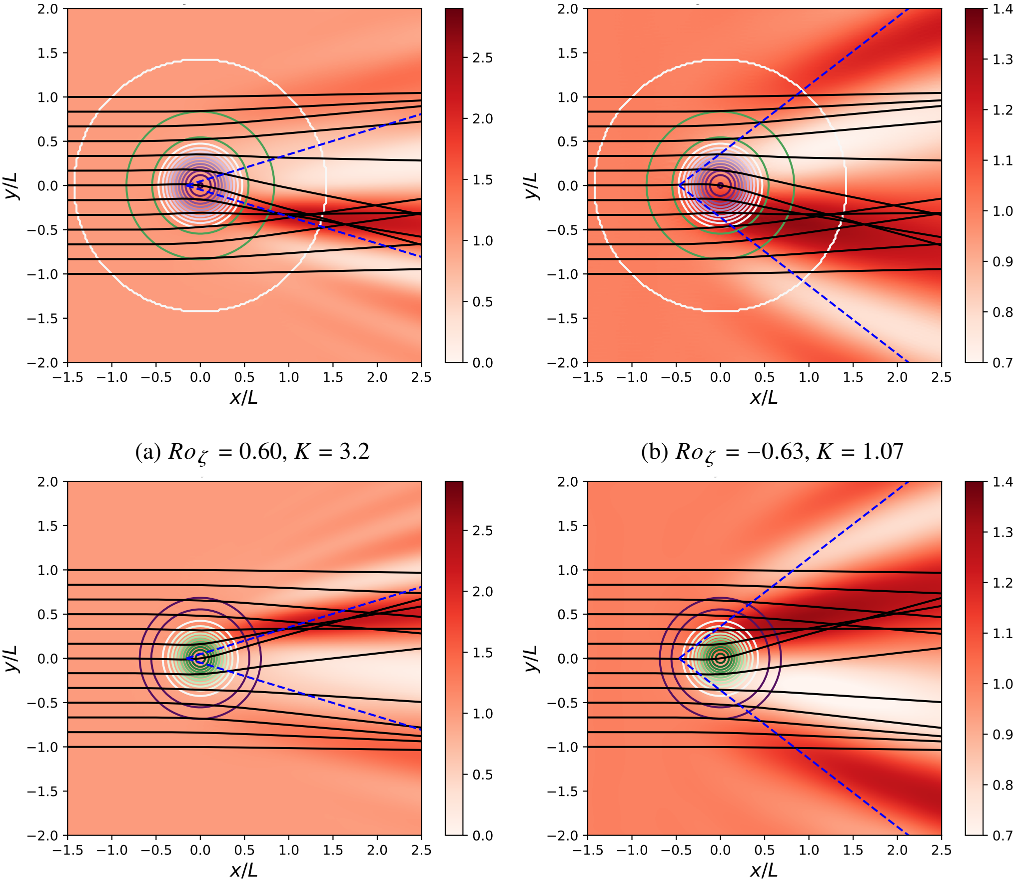

(a) $Ro_\zeta = 0.60$, $K = 3.2$

(b) $Ro_\zeta = -0.63$, $K = 1.07$

(c) $Ro_\zeta = -0.63$, $K = 3.2$

(d) $Ro_\zeta = 0.60$, $K = 1.07$

Figure 4: Full flux field $\overline{\boldsymbol{\phi}}_w$ for two similar but opposite-signed $Ro_\zeta$ and two wavelengths, see sub-captions. $Bu = 0.88$ in all cases. Ray-tracing lines are in black. The green and purple contours correspond to the colourbar shown in figure 1a. The two dashed blue lines represent the primary scattering angle predicted by triad resonance theory.

anticyclonic vortex centre rises above the mean depth, and since the group speed,

$$c_g = \frac{ghk}{(f^2 + ghk^2)^{1/2}}, \tag{3.1}$$

increases with depth, the waves travel faster through the centre of the vortex, and thus the height effects make the waves curve away from the centre line $y = 0$. Oppositely, cyclonic vortex centres dip below the mean depth, thus height effects make waves curve towards the centre line. We checked that this effect is an order of magnitude smaller than the vorticity effect for balanced vortices.

The exact location where the rays converge aligns more closely with constructive interferences between CSB, LSB, and RSB, for $K = 3.2$ as opposed to $K = 1.07$. Note that the ray tracing predictions do not vary much for the range of $K$ explored. Figure 4 reveals that the most striking limitation of ray tracing is that it does not capture the broad angles of scattering, as can be seen from the interference pattern created by the incoming wave and scattered waves.

The TRT formalism of Ward & Dewar (2010) can be used to predict the principal scattering angle, $\theta_p$, that is, the angle made between the incoming wave with wave vector $\boldsymbol{k}_i$, and the scattered wave $\boldsymbol{k}_s$, which is determined by the main length scale in the vortex $\boldsymbol{k}_v = 2\pi/L_a$. Assuming $|k_i| = |k_s|$ the principal angle can be calculated as a function of $K$ as

$$\theta_p = 2\arcsin((2K)^{-1}). \tag{3.2}$$

This implies that the angle of scattering would increase for smaller $K$. For $K = 1.07$, triad resonance predicts that if there was only one balanced length scale $L_a$, the angle of scattering would be 65°, which is more than what we measure in our experiments as shown in figure 4. We expect the discrepancy to be due to the multiple length scales and spatial variations of the vorticity field experienced by the part of the plane wave passing through the centre. Thus, even in this simple case, the principal scattering angle is not enough to describe this pattern. Moreover, non-resonant, higher-order interactions would not be captured by TRT. Thus, neither ray tracing nor triad resonances easily predict the exact nature of the scattering pattern in this simple set-up.

| | $A$ | $\alpha$ | $\beta$ | $\gamma$ |
|---|---|---|---|---|
| Anticyclonic | $10.67 \pm 0.19$ | $2.13 \pm 0.01$ | $-0.98 \pm 0.01$ | $2.10 \pm 0.01$ |
| Cyclonic | $5.35 \pm 0.21$ | $1.94 \pm 0.01$ | $-1.13 \pm 0.01$ | $2.10 \pm 0.01$ |
| Combined | $9.78 \pm 0.59$ | $2.10 \pm 0.02$ | $-0.99 \pm 0.01$ | $2.02 \pm 0.02$ |

Table 2: Optimisation parameters and their standard deviations for equation (3.3).

### 3.2. *Scattering Statistics*

We now summarise the relationship between the scattered ratio $S$ on the non-dimensional numbers $Bu$, $K$, as well as one of the three vortex strength metrics $Ro_b$, $Ro_\zeta$, $\varepsilon$. Visual inspection reveals that for small values of the non-dimensional parameters, the scattering ratio follows power law relations, while for large values, the scattering ratio approaches a maximum of 100% conversion. Therefore, we propose to use a sigmoidal relationship that is linear near the origin, and tends to a positive constant towards infinity. We considered several functions, none of which demonstrated superior performance, and settled on

$$S_Z^\theta = \frac{2}{\pi} \arctan(A Z^\alpha Bu^\beta K^\gamma), \tag{3.3}$$

where the superscript $\theta$ denotes the optimised fit, $Z \in \{|Ro_b|, |Ro_\zeta|, \varepsilon\}$ is a placeholder for the three metrics of vorticity we will test, and where $A$, $\alpha$, $\beta$ and $\gamma$ are the optimisation parameters. To find them, we fit the cyclonic experiments separately from the anticyclonic experiments, and in parallel, for comparison, we fit both datasets together, hereafter referred to as the "combined case". We use the least squares method to find the optimisation parameters using $Z = |Ro_b|$ which we show in table 2. We find that all the optimisation parameters have small errors, indicating that our fitting function is appropriate. The combined case is plotted in figure 5, where we have re-scaled the data based on the fit parameters. We see that anticyclonic vortices scatter energy at a slightly higher rate, as noted by the data points being

| | $A$ | $\alpha$ | $\beta$ | $\gamma$ |
|---|---|---|---|---|
| $Ro_b$ | $9.78 \pm 0.59$ | $2.10 \pm 0.02$ | $-0.99 \pm 0.01$ | $2.02 \pm 0.02$ |
| $\mathrm{Ro}_\zeta$ | $0.057 \pm 0.001$ | $1.77 \pm 0.02$ | $-1.02 \pm 0.01$ | $2.05 \pm 0.02$ |
| $\varepsilon$ | $0.47 \pm 0.02$ | $1.03 \pm 0.01$ | $-0.98 \pm 0.01$ | $2.02 \pm 0.02$ |

Table 3: Optimisation parameters using three different vortex strength metrics in place of the bulk Rossby number in equation (3.3).

slightly above the line of perfect fit, and as confirmed by table 2. However, the distinction is too small to conclusively claim that this is physical. Thus, we hereafter focus on the combined cases.

We now redo the optimisation using the enstrophy $\varepsilon$ and the vorticity Rossby number $Ro_\zeta$ in addition to the bulk Rossby number $Ro_b$. The optimisation parameters for the three vortex strength metrics are shown in table 3. Figure 5 shows the three combined fits scaled by their respective parameters. They appear to be approximately equivalent; however, if we plot the same data on a logarithmic scale (figure 6), we observe that using the vorticity Rossby number $Ro_\zeta$ is not as effective as using enstrophy $\varepsilon$ or bulk Rossby number $Ro_b$, which yield closer fits to data points. Both seem to result in round number scaling for $\alpha$ as well, with $\alpha \approx 2$ if $Z = \mathrm{Ro}_b$, or $\alpha \approx 1$ if $Z = \varepsilon$. No matter which measure of vortex strength we use, we find that $\beta \approx 2$ and $\gamma \approx -1$. Simplifying the dependencies of $S$ further, notice that

$$Ro_b/\sqrt{Bu} = U/\sqrt{gH} = U/c_0 = Fr, \tag{3.4}$$

where the last number is the Froude number.

Collecting these approximations, we find that for small values of our non-dimensional parameters, equation (3.3) simplifies into

$$S \approx 5Fr^2K^2, \tag{3.5}$$

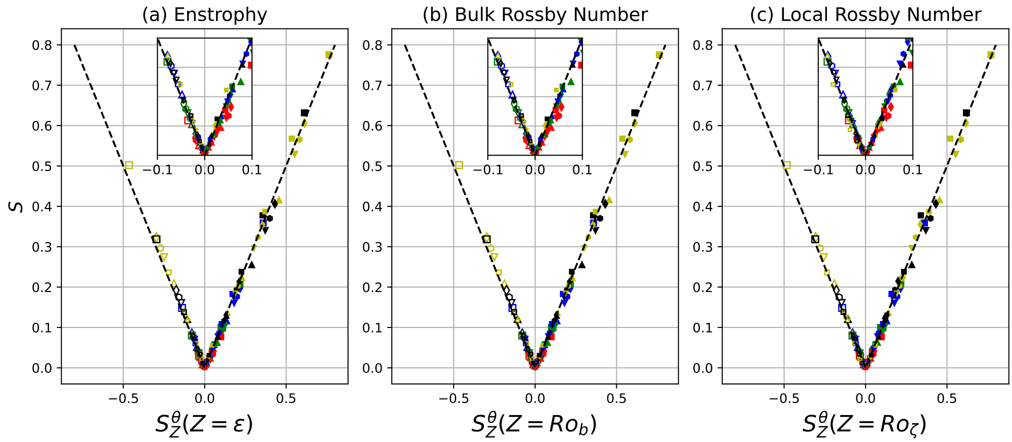


Figure 5: The $x$-axis shows the the data scaled by the fit function and respective optimisation parameters for the (a) enstrophy (b) bulk Rossby Number, (c) vorticity Rossby number. The size of the markers corresponds to the bulk Rossby number, the colours correspond to the adjusted ratio of length scales, and the markers correspond to unadjusted Burger number, as shown in the legend in figure 6. The black dashed lines are perfect fit lines.

which we find to be reasonably accurate up to $S \approx 0.2$ (see figure 7). This simplified equation breaks down the scattering into a ratio of velocities multiplied by the ratio of length scales.

## 4. Discussion and Conclusion

We examined the scattering effect induced by an isolated vortex on a plane Poincaré wave. By removing the vortex and the incoming wave, we are able to visualise the scattered wave energy using the wave-averaged flux. The scattered energy forms in a “left, right, left” (“right,, left, right”) pattern, which we attribute to the strong negative (positive) vorticity in the interior for (anti)cyclones, and weaker positive (negative) vorticity in the exterior. The ray-tracing equations capture this alternating pattern, but the locations of ray convergence do not always align with the locations of maximum amplitude in the simulation data. We see the expected limitations of ray tracing when the vortex and wavelength are of comparable size,

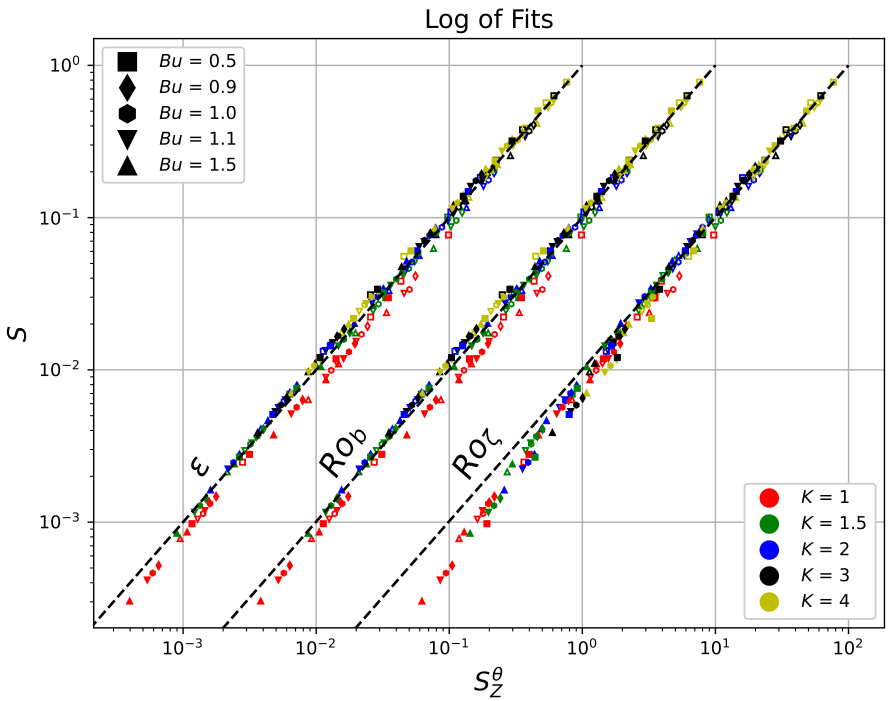


Figure 6: The scattering ratio data in figure 5 shown in logarithmic scale. The black dashed lines show perfect fits.

most strikingly when $K = 1$ where the angle of scattering it predicts is much shallower than those we see in the simulations. The scattering pattern of anticyclonic and cyclonic vortices of similar Rossby number magnitude lead to slightly different patterns due to the difference in shape after cyclogeostrophic balance, but the effect is minor in our parameter regime.

Using three-dimensional fits, we derived a relation that gives the scattering ratio as a function of $Bu$, $K$, and a measure of the vortex strength. We observe that the fit is successful when an arctan is used with a power law combination of the three non-dimensional numbers as the argument. The bulk Rossby number $Ro_b$ and enstrophy $\varepsilon$ are the most suitable vortex strength metrics to predict the scattering ratio, while the vorticity Rossby number $Ro_\zeta$ yields a less suitable approximation. For low values of $S$, $S \propto Ro_b^2 \propto Ro_\zeta^{1.77} \propto \varepsilon$. Smaller

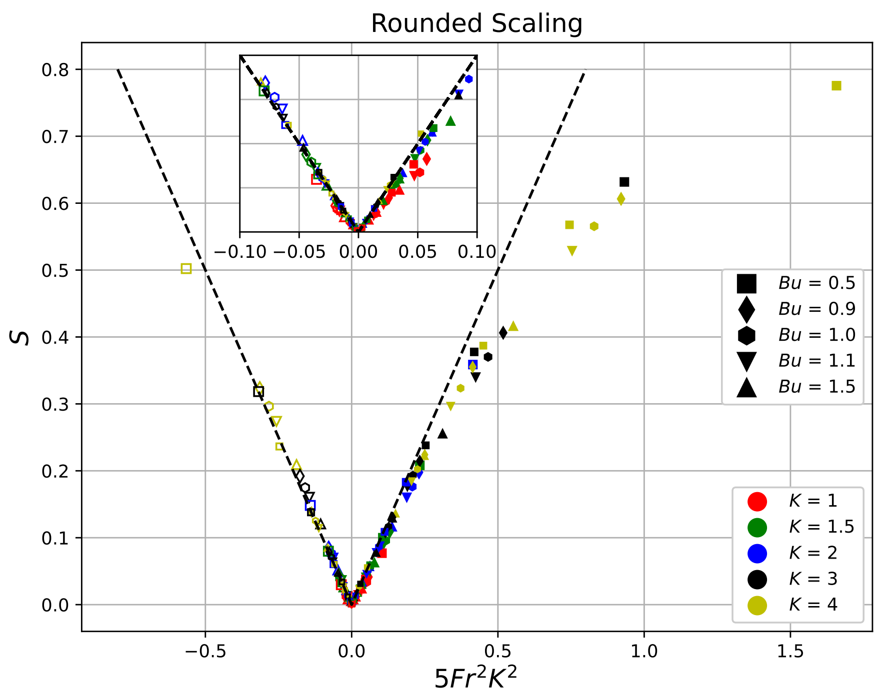


Figure 7: Simplified scaling for low scattering ratios as a function of only the Froude number $Fr = Ro_b/\sqrt{Bu}$ and length scales ratio $K$.

wavelengths lead to higher scattering ratios, with $S \propto K^2$, which would correspond to higher vertical modes and frequencies for ITs. This aligns with the intuition that short-scale variations in the medium will not affect a larger wavelength. The dependence of $S \propto Bu^{-1}$ implies that the faster the wave moves through the vortex, the less it will be scattered. Although we did not vary $Fr_w$, we do not anticipate the results to vary until the wave has enough energy to alter the structure of the vortex itself (e.g., via wave capture; Bühler & McIntyre 2005), or to undergo destabilising non-linear processes. For small scattering ratios, we discovered a straightforward relation that combines the Rossby number and Burger number into the Froude number. This has the advantage of reducing the scattering ratio as a function of the ratio of the velocity scales $Fr$ multiplied by the ratio of the length scales

$K$. Independently, Ito & Nakamura (2023) show that $FrK = \frac{U}{c_0}\frac{L}{\lambda}$ can be used to separate the vortical effects on the wave from the linear equations. They vary this parameter as a whole to show different scattering regimes and patterns. At higher values, they show that the wave can become trapped in the vortex, which may lead to the plateau that we see in our scalings. A similar ratio to $FrK$ also appeared in Coste *et al.* (1999), which investigates how a vertical vortex in solid-body rotation creates phase dislocations on an incoming wave.

The parameter range we explored covers a broad range of physical regimes in which an IT will interact with eddies in the ocean. We did not explore waves larger than the vortices, but we can extrapolate from our data that $K < 1$ would lead to little scattering ($S < 0.1$) even at vorticity Rossby numbers of $O(1)$ and Burger numbers of $O(0.1)$. We also did not explore simulations with $|Ro_\zeta| \gg 1$ and $Bu < 0.4$, but since we came close to complete scattering with $K = 4$, we can extrapolate to find which simulations would lead to completely scattered waves ($S = 1$). For example, if we had Rossby and Burger numbers equal to one, a wave with $K = 5$ would already lead to almost complete scattering with $S = 0.97$. In open ocean regimes, mesoscale eddies are about the size of mode-1 $M_2$ tides ($K = 1$) and have $Ro_b = 0.01$ and $Bu \approx 1$, so we predict that the scattering will be small at $S < 1\%$. In submesoscale regimes, near coasts and strong currents, where mode 5 ITs interact with vortices of $Ro_b > 0.1$, the scattering ratio will be $> 10\%$. These results inspire useful diagnostics for satellite altimetry data and global circulation models to determine where errors may be at their highest given the local vorticity field, IT mode, local rotation rate, and stratification. Future work on our idealised model should include simple time-varying balanced flows (e.g., vortex pairs), oblate vortices, and adding vertical layers to include the effects of baroclinicity in the balanced flow.

## Appendix A. Cyclogeostrophic Balance Iterative Method

To create a time-independent balanced vortex with a non-zero Rossby number we need to include the effects of advection. Thus, the vortex must satisfy ,

$$\boldsymbol{u} \cdot \nabla \boldsymbol{u} + f\hat{\boldsymbol{z}} \times \boldsymbol{u} = -g\nabla\eta. \tag{A 1}$$

Equation A 1 can be solved analytically for some axis-symmetric cases; however, we can extend this to larger $Ro$ if we use the iterative method in Penven *et al.* (2014), which we describe below.

Let the velocity $\boldsymbol{u_g}$ associated with the geostrophic flow be $f\hat{\boldsymbol{z}}\times\boldsymbol{u_g} = -g\nabla\eta$. We rearrange equation A 1 to give

$$\boldsymbol{u} - \hat{\boldsymbol{z}}f^{-1} \times (\boldsymbol{u} \cdot \nabla \boldsymbol{u}) = \boldsymbol{u_g}. \tag{A 2}$$

It is then possible to approximate the solution by iterating equation A 2 as follows,

$$\boldsymbol{u}^{(n+1)} = \boldsymbol{u_g} + \hat{\boldsymbol{z}}f^{-1} \times (\boldsymbol{u}^{(n)} \cdot \nabla \boldsymbol{u}^{(n)}) \tag{A 3}$$

while $\max|\boldsymbol{u}^{(n+1)} - \boldsymbol{u}^{(n)}| < 10^{-4}ms^{-1}$ or until $\boldsymbol{u}^{(n+1)} > \boldsymbol{u}^{(n)}$. These adjusted velocities are used to initialise the velocity field in the vortex simulation.

## Appendix B. Sponge layers

The Tukey window is used to force and absorb waves on either side of the domain. It has the profile of a tapered cosine at the edges and a constant at the center. This is useful to ensure that the waves achieve the amplitude they are prescribed.

The formula for the Tukey window is shown below,

$$\Pi(x, x_0) = \begin{cases} 0 & x < x_0 \\ \frac{1}{2}\left\{1 - \cos\left[\frac{2\pi x}{\Delta\lambda}\right]\right\} & x_0 \leqslant x < \Delta\lambda/2 + x_0 \\ 1 & \Delta\lambda/2 + x_0 \leqslant x < \lambda - \Delta\lambda/2 + x_0, \\ \frac{1}{2}\left\{1 - \cos\left[\frac{2\pi x}{\Delta\lambda} - \frac{2\pi}{\Delta}\right]\right\} & \lambda - \Delta\lambda/2 + x_0 \leqslant x < \lambda + x_0, \\ 0 & \lambda + x_0 \leqslant x, \end{cases} \tag{B 1}$$

where $\Delta = 0.7$.

The vortex adjustment simulation requires a sponge layer to absorb the waves that radiate during the adjustment process. To absorb waves with minimal reflection, a circular sponge layer is set at a distance $R_1 = 2L$, which increases linearly until $R_2 = 2.8L$ as shown below.

$$CS(r) = \begin{cases} 0 & r \leqslant R_1, \\ (r - R_1)/(R_2 - R_1) & R_1 \leqslant r \leqslant R_2, \\ 1 & R_2 \leqslant r. \end{cases} \tag{B 2}$$

For simulations with high Rossby numbers, there does tend to be some reflection, but has a small effect on the diagnostics.

## Appendix C. Linear Shallow Water Equations

The linear shallow-water equations are as follows,

$$\partial_t \boldsymbol{u} + f\hat{z} \times \boldsymbol{u} = -g\nabla\eta \qquad \text{and} \qquad \partial_t h + H\nabla \cdot (\boldsymbol{u}) = 0, \tag{C 1}$$

where $f$ is constant in this article. Let us assume a wave solution that is only propagating in one direction, so that $\boldsymbol{V} = [\tilde{u}, \tilde{v}, \tilde{h}]e^{ikx}$ we can then rewrite equations C 1 as

$$\partial_t \boldsymbol{V} + \boldsymbol{M}\boldsymbol{V} = 0, \qquad \text{where} \qquad \boldsymbol{M} = \begin{bmatrix} 0 & -f & ikg \\ f & 0 & 0 \\ ikH & 0 & 0 \end{bmatrix}. \tag{C 2}$$

The three eigenvalues of $M$ are proportional to the frequencies of the wave modes. They are $\omega_G = 0$ and $\omega_W^{(\pm)} = \pm\sqrt{f^2 + gHk^2}$, with corresponding eigenvectors

$$G = \left[0,\ 1,\ -\frac{if}{gk}\right] \qquad \text{and} \qquad W_\pm = \left[\frac{\omega_W^{(\pm)}}{f},\ 1,\ \frac{-ikH}{f}\right]. \tag{C 3}$$

The eigenvectors $W_\pm$ are used to force the wave from the right.

## Appendix D. Ray Tracing

Ray tracing is a method to track the position and wavevector of a wavepacket through a fluid media, assuming that the wavelength is small compared to the length scales in the media. Let the position of the wavepacket be $\boldsymbol{x}$ with wavevector $\boldsymbol{k}$, and it made to pass through a velocity field $\boldsymbol{U} = (U, V)$, then the ray tracing equations read,

$$d\boldsymbol{x}/dt = U + d\omega/d\boldsymbol{k} \qquad \text{and} \qquad d\boldsymbol{k}/dt = -(\boldsymbol{\nabla}\boldsymbol{U}) \cdot \boldsymbol{k} - d\omega/d\boldsymbol{x}, \tag{D 1}$$

where $\omega = \sqrt{f^2 + gh\boldsymbol{k}^2}$. The first equation describes the evolution of the wave packet position due to the advection of the media and the group speed. The second equation describes the refraction of the wave vector as a result of strain and shear and due to the change in frequency.

### REFERENCES

Bartello, P. 1995 Geostrophic adjustment and inverse cascades in rotating stratified turbulence. *Journal of the Atmospheric Sciences* **52** (24), 4410–4428.

Bühler, Oliver 2014 *Waves and Mean Flows*. Cambridge University Press.

Bühler, Oliver & McIntyre, Michael E. 2005 Wave capture and wave-vortex duality. *Journal of Fluid Mechanics* **534**, 67–95.

Burns, Keaton J., Vasil, Geoffrey M., Oishi, Jeffrey S., Lecoanet, Daniel & Brown, Benjamin P. 2020 Dedalus: A flexible framework for numerical simulations with spectral methods. *Physical Review Research* **2** (2), 023068.

Chavanne, C., Flament, P., Luther, D. & Gurgel, K-W. 2010 The Surface Expression of Semidiurnal Internal Tides near a Strong Source at Hawaii. Part II: Interactions with Mesoscale Currents*. *Journal of Physical Oceanography* **40** (6), 1180–1200.

Coste, Christophe, Lund, Fernando & Umeki, Makoto 1999 Scattering of dislocated wave fronts by vertical vorticity and the Aharonov-Bohm effect. I. Shallow water. *Physical Review E* **60** (4), 4908–4916.

Dunphy, Michael & Lamb, Kevin G. 2014 Focusing and vertical mode scattering of the first mode internal tide by mesoscale eddy interaction. *Journal of Geophysical Research: Oceans* **119** (1), 523–536.

Egbert, G. D. & Ray, R. D. 2000 Significant dissipation of tidal energy in the deep ocean inferred from satellite altimeter data. *Nature* **405** (6788), 775–778.

Egbert, Gary D. & Ray, Richard D. 2003 Semi-diurnal and diurnal tidal dissipation from TOPEX/Poseidon altimetry. *Geophysical Research Letters* **30** (17), n/a–n/a.

Fu, Lee-Lueng, Christensen, Edward J., Yamarone, Charles A., Lefebvre, Michel, Ménard, Yves, Dorrer, Michel & Escudier, Philippe 1994 TOPEX/POSEIDON mission overview. *Journal of Geophysical Research: Oceans* **99** (C12), 24369–24381.

Garrett, Chris & Kunze, Eric 2007 Internal Tide Generation in the Deep Ocean. *Annual Review of Fluid Mechanics* **39** (1), 57–87.

Ito, Kaoru & Nakamura, Tomohiro 2023 Three Regimes of Internal Gravity Wave–Stable Vortex Interaction Classified by a Nondimensional Parameter $\delta$: Scattering, Wheel-Trapping, and Spiral-Trapping with Vortex Deformation. *Journal of Physical Oceanography* **53** (4), 1087–1106.

Kafiabad, Hossein A., Savva, Miles A. C. & Vanneste, Jacques 2019 Diffusion of inertia-gravity waves by geostrophic turbulence. *Journal of Fluid Mechanics* **869**, R7.

de Lavergne, C., Falahat, S., Madec, G., Roquet, F., Nycander, J. & Vic, C. 2019 Toward global maps of internal tide energy sinks. *Ocean Modelling* **137**, 52–75.

Lelong, M. Pascale & Riley, James J. 1991 Internal wave—vortical mode interactions in strongly stratified flows. *Journal of Fluid Mechanics* **232** (-1), 1.

McWilliams, James C. 2016 Submesoscale currents in the ocean. *Proceedings of the Royal Society A: Mathematical, Physical and Engineering Sciences* **472** (2189), 20160117.

Morrow, Rosemary, Fu, Lee-Lueng, Ardhuin, Fabrice, Benkiran, Mounir, Chapron, Bertrand, Cosme, Emmanuel, D'Ovidio, Francesco, Farrar, J. Thomas, Gille, Sarah T., Lapeyre, Guillaume, Le Traon, Pierre-Yves, Pascual, Ananda, Ponte, Aurélien, Qiu, Bo, Rascle, Nicolas, Ubelmann, Clement, Wang, Jinbo & Zaron, Edward D. 2019 Global Observations of Fine-Scale Ocean Surface Topography With the Surface Water and Ocean Topography (SWOT) Mission. *Frontiers in Marine Science* **6**.

Nash, Jonathan, Shroyer, Emily, Kelly, Samuel, Inall, Mark, Duda, Timothy, Levine, Murray, Jones, Nicole & Musgrave, Ruth 2012 Are Any Coastal Internal Tides Predictable? *Oceanography* **25** (2), 80–95.

Penven, Pierrick, Halo, Issufo, Pous, Stéphane & Marié, Louis 2014 Cyclogeostrophic balance in the Mozambique Channel. *Journal of Geophysical Research: Oceans* **119** (2), 1054–1067.

Rainville, Luc & Pinkel, Robert 2006 Propagation of Low-Mode Internal Waves through the Ocean. *Journal of Physical Oceanography* **36** (6), 1220–1236.

Savva, M.A.C., Kafiabad, H.A. & Vanneste, Jacques 2021 Inertia-gravity-wave scattering by three-dimensional geostrophic turbulence. *Journal of Fluid Mechanics* **916**, A6, arXiv: 2008.02203.

Savva, Miles A. C. & Vanneste, Jacques 2018 Scattering of internal tides by barotropic quasigeostrophic flows. *Journal of Fluid Mechanics* **856**, 504–530.

Shakespeare, Callum J. 2016 Curved Density Fronts: Cyclogeostrophic Adjustment and Frontogenesis. *Journal of Physical Oceanography* **46** (10), 3193–3207.

Ward, Marshall L. & Dewar, William K. 2010 Scattering of gravity waves by potential vorticity in a shallow-water fluid. *Journal of Fluid Mechanics* **663**, 478–506.

Zhao, Zhongxiang, Alford, Matthew H., Girton, James B., Rainville, Luc & Simmons, Harper L. 2016 Global Observations of Open-Ocean Mode-1 M2 Internal Tides. *Journal of Physical Oceanography* **46** (6), 1657–1684.

Declaration of Interests. The authors report no conflict of interest.